

Relative astrometry of the $J=1\rightarrow 0$, $v=1$ and $v=2$ SiO masers towards R Leonis Minoris using VERA

María J. RIOJA^{1,2} Richard DODSON^{1,2} Ryuichi KAMOHARA³

Francisco COLOMER² Valentín BUJARRABAL² and Hideyuki KOBAYASHI³

¹*School of Physics, University of Western Australia, Australia*

²*OAN, Alcalá de Henares, Madrid, Spain*

³*VERA Project Office, NAOJ, Mitaka, Tokyo, Japan*

mj.rioja@oan.es

(Received 2008 0; accepted 2008 0)

Abstract

Oxygen-rich Asymptotic Giant Branch (AGB) stars are intense emitters of SiO and H₂O maser lines at 43 ($J=1\rightarrow 0$, $v=1$ and 2) and 22 GHz, respectively. VLBI observations of the maser emission provides a unique tool to sample the innermost layers of the circumstellar envelopes in AGB stars. Nevertheless, the difficulties in achieving astrometrically aligned $v=1$ and $v=2$ SiO maser maps have traditionally prevented a unique interpretation of the observations in terms of physical underlying conditions, which depend on the nature of the SiO pumping mechanism. We have carried out observations of the SiO and H₂O maser emission towards RLMi, using the astrometric capabilities of VERA. Due to the too-weak emission of the reference calibrator we had to develop a special method to accurately relate the coordinates for both transitions. We present relative astrometrically aligned $v=1$ and $v=2$ $J=1\rightarrow 0$ SiO maser maps, at multiple epochs, and discuss the astrophysical results. The incorporation of astrometric information into the maps of SiO masers challenges the weak points in the current theoretical models, which will need further refinements to address the observations results.

Key words: Stars: AGB and post-AGB – Stars: circumstellar matter – Stars: late-type – Masers (SiO) – VERA

1. Introduction

O-rich AGB stars are intense emitters of SiO and H₂O maser lines, particularly at 43 (SiO lines, $J=1\rightarrow 0$, $v=1$ and 2) and 22 GHz (H₂O, $J_{K-,K+}=6_{1,6}-5_{2,3}$). SiO masers require a very high excitation and appear at a distance of a few stellar radii, $\sim 10^{14}$ cm, occupying a more or less circular structure. H₂O emission is found further from the star, $\sim 10^{15}$ cm, with less well defined structures. A combined study of both masers should then produce a very accurate

description of the structure and kinetics of these inner layers. In such inner circumstellar shells, from which the whole circumstellar envelope will be formed, the dust grains are still growing and the gas has not yet attained its final expansion velocity, since expansion is supposed to be powered by radiation pressure onto grains. The dynamics in the SiO emitting region is dominated by pulsation, which propagates from the photosphere via shocks, and by the first stages of outwards acceleration. Their study is therefore basic in understanding the mass loss process and the envelope formation in AGB stars.

The relative positions of the spots of both $v=1$ and $v=2$ SiO transitions are an important result in order to elucidate the nature of the pumping mechanisms (Humphreys et al. 2002, Bujarrabal 1994). Existent maps suggest that the spots of these lines are systematically separated by a few milliarcsecond (mas), (Desmurs et al. 2000, Yi et al. 2005, Boboltz & Wittkowski 2005). In the former, the authors have explained why we believe this favors radiative mechanisms, but we note that Yi et al. found similar offsets, but also many common features, which they argued supported the collisional model. A few attempts to study theoretically the observed spatial distribution of the different SiO masers have been published, see the short report on collisional pumping predictions for the relative distribution of $v=1,2 J=1\rightarrow 0$ and $v=1 J=2\rightarrow 1$ masers by Humphreys et al. (2000), and the predictions for the same parameters from radiative models by Soria-Ruiz et al. (2004), including in this case the effects of line overlap. However, existing models are not sophisticated enough to undertake a sensible explanation of present high-quality maps of SiO maser emission, as we will discuss in Sect. 4.

Our understanding of these problems has greatly changed from the first empirical comparisons between conventional VLBI observations, which do not provide us with absolute coordinates. Accordingly, the location and shape of the maser regions, one with respect to the other and with respect to the star's position [very accurately measured for many AGB stars, with Hipparcos satellite (Perryman et al. 1997) with a typical precision of 1 mas], are still not well known. The studies of SiO and H₂O maser spot distributions are therefore severely hampered by the lack of accurate information on the absolute coordinates in the maps of the different lines.

The dual-beam interferometer VERA is very well suited to produce VLBI maps with accurate absolute astrometry, thanks to the dual-beam design that enables simultaneous observation of the maser line and a reference continuum source (in general, a quasar), and its inherent instrumental phase stability. This approach relies on the detectability of the reference source, which in practice can be problematic. In the observations presented in this paper absolute astrometry with respect to a celestial reference frame was not possible due to the weakness of the simultaneously observed reference continuum source. We present here multi-epoch VERA observations of SiO and H₂O maser emission in the well known Mira-variable R LMi, and the relative alignment of $v=1$ and $v=2 J=1\rightarrow 0$ SiO maser emission derived from an astrometric analysis.

We describe our data reduction procedure to partially recover astrometric information, even when there are no frequent observations of a reference source. This method is applied to our observations of RLMi, and was shown to be useful to measure the relative positioning of both SiO maser lines. Results from the analysis of four different epochs of observations are presented.

RLMi is an O-rich Mira-type variable, with a pulsation period of about 373 days and a spectral type ranging between M6.5, at the optical maximum, and M9.0, at the minimum. Its distance is assumed to be ~ 350 pc from the well-known period-luminosity relation, the Hipparcos parallax measurement being poor (see Whitelock et al., 2000). RLMi is a well known emitter in SiO masers, it was in particular accurately monitored by Pardo et al. (2004), who found the periodic variation in-phase with the IR cycle typical of Mira-type stars. However, accurate VLBI maps of SiO masers in RLMi had not been reported up to date.

The contents of the paper are organized as follows. The observational setup is described in Sect. 2. In Sect. 3 we describe the special data reduction strategy used to preserve the relative astrometry between the two SiO maser transitions. In Sect. 4 we present the resulting maps and discuss the astrophysical results.

2. Observations

We carried out a series of VERA observations at 5 epochs of the SiO maser emission ($v=1$ and $v=2$ $J=1\rightarrow 0$), at 43 GHz, and 3 epochs of observations of H₂O maser emission, at 22 GHz, towards RLMi, between October 2006 and May 2007. Of these, four epochs of SiO and one epoch of H₂O maser observations have been completely analyzed, and the results are presented in this paper. Table 1 lists the epoch and duration of the observations along with the stellar phases, as derived from the optical light curve shown in Fig. 1.

At all epochs the observations were made in the dual-beam mode, with the 4 VERA antennas (Mizusawa, Iriki, Ishigaki-jima, and Ogasawara) observing simultaneously RLMi and a nearby continuum reference source (J0945+3534 or J0952+3512) for ~ 8 -9 hours. Every hour, a ~ 5 min scan on a bright continuum fringe-finder calibrator source, 4C39.25 (J0927+3902), was included.

The observations were performed with the DIR2000 recording system at a data rate of 1 Gbps. Each antenna recorded an aggregate of 256 MHz bandwidth, using 2-bit Nyquist sampling, subdivided into a total of 16 IF channels for both beams. During the observations at 43 GHz, two 16-MHz channels were allocated to the observations of the two SiO maser transitions with one beam (beam A). The IF channels were tuned to match the Doppler-shifted frequencies of the $v=2$, $J=1\rightarrow 0$ (rest frequency 42.820584 GHz) and the $v=1$, $J=1\rightarrow 0$ (rest frequency 43.122027 GHz) line transitions. The remaining fourteen 16-MHz IF channels were devoted to the simultaneous observations of the continuum source on the other beam (beam B), evenly distributed over the ~ 300 MHz frequency gap between the two maser transitions.

Table 1. Details on the SiO and H₂O maser observations towards RLMi with VERA.

| Epoch | Year/DOY | Duration (UT) | Stellar Phase |
|------------------|----------|---------------|---------------|
| SiO | | | |
| I | 2006/298 | 18:30-02:30 | $\phi = 0.84$ |
| II | 2007/014 | 12:30-21:30 | $\phi = 0.07$ |
| III | 2007/106 | 06:30-15:30 | $\phi = 0.32$ |
| IV | 2007/133 | 05:00-14:00 | $\phi = 0.40$ |
| H ₂ O | | | |
| | 2007/132 | 05:00-14:00 | $\phi = 0.40$ |

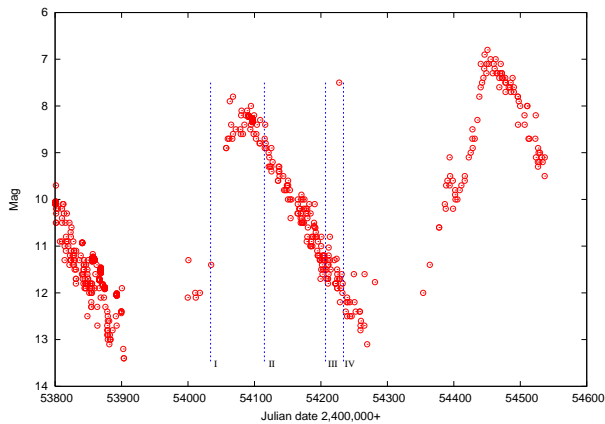


Fig. 1. Stellar optical light curve for RLMi (courtesy of AAVSO). The vertical lines mark the epochs of the SiO maser observations, with VERA, presented in this paper.

During the 22 GHz observations, only one 16-MHz IF channel (centered on 22.3512 GHz) was allocated to the observations of the H₂O maser emission (beam A). The other fifteen IF channels were allocated to the simultaneous observations of the continuum source with the other beam (beam B).

The correlation was done at the Mitaka FX correlator (Chikada et al. 1991) with a spectral resolution of 512 channels per IF for beam A, and 64 channels per IF for beam B. At a single epoch, output data sets were generated for each beam, consisting of the visibility functions averaged to 1 second, with samples every 31.25 kHz in frequency, yielding velocity resolutions of 0.22 km s⁻¹ and 0.4 km s⁻¹ for the line observations at 43 and 22 GHz, respectively.

3. Data reduction

The “conventional” phase referencing analysis strategy with VERA consists of transferring phase/delay/rate solutions, from the data reduction of observations of the reference source on one beam to the simultaneous observations of the target source on the other beam. The

calibrated visibilities of the target source are Fourier transformed without further calibration to yield synthesis images, which preserve the astrometric information with respect to an external reference.

Unfortunately, the continuum reference source in our observations was too weak to be detected using self-calibration techniques, at either of the frequencies, and hence prevented us from following the “conventional” analysis route. Some authors have performed the “inverse” analysis, and used the data from the line source to enhance the detection of a weak continuum reference source (Choi, Kamohara, priv. comm.); this approach also failed in our observations.

The lack of detection of the continuum reference source prevents us from achieving our initial goal, that is measuring absolute positions of all the maser maps, i.e. the H₂O (22 GHz) and two SiO (43.1 GHz and 42.8 GHz) maser transitions, with respect to an external reference, and with respect to the star. Instead, we have followed a different analysis strategy that allows the measurement of the alignment between multiple transitions simultaneously observed, even in cases when the reference source is not detected, using the interleaved observations (\sim every hour) of the primary calibrator source, 4C39.25, 5.9 $^\circ$ away. Our proposed analysis route preserves the relative positions between the two SiO maser maps at each single epoch, but we can not recover the astrometry with respect to the external continuum source on beam B, thus preventing comparison between different epochs and with respect to the H₂O maser maps.

We used the NRAO AIPS software package for the data reduction. The information on measured system temperatures, telescope gains, and estimated bandpass corrections at the individual antennae were used to calibrate the raw correlation coefficients of the calibrator and, along with Doppler corrections, of the line source observations. Then we used the AIPS task FRING, which is a global self-calibration algorithm, to estimate residual antenna-based VLBI phases and its partial derivatives with respect to frequency (hereafter group delay, τ), and time (hereafter rate), on the calibrator data set. These terms result from unaccounted contributions from the atmospheric propagation and from errors in the array geometry during the data processing.

An advantage of the digital filters in the VERA DIR2000 recording system is the absence of instrumental phase term offsets introduced by the electronics at each IF, which enables the straight-forward use of all the IFs as an effective bandwidth for the estimation of a more precise group delay (since $\sigma_\tau \propto 1/\text{bandwidth}$). For arrays with independent IF electronics a further stage of calibration would be required. Fig. 2 shows an example of the slow temporal variation of the estimated group delays for the calibrator source 4C39.25, at one of the epochs of observations and for all VERA antennas. These residual group delays measure the rate of change of the phase with frequency, and hence the phase difference ($\Delta\phi$) between IFs separated by a bandwidth $\Delta\nu$ is given by $\Delta\phi = 2\pi \Delta\nu \tau(t)$. The stability of the system allows us to use observations of a calibrator made every hour or so – much less frequently than Yi et al.. The scarcity of calibrator scans requires us to take great care with the interpolation of the phase

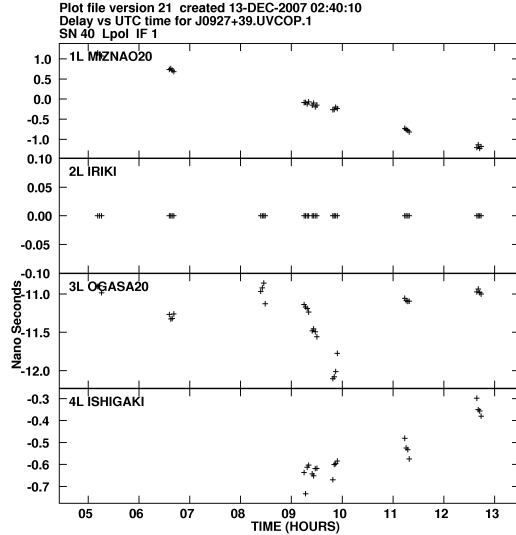


Fig. 2. Temporal variation of residual VERA group delays estimated from the analysis of 4C39.25 observations at 43 GHz, with FRING, for epoch IV. These introduce different phase ambiguities at each IF.

from the group delay solutions.

In the analysis of the RLMi data set we used the interpolated values of the calibrator group delays to the times of the line observations to remove the “instrumental” long term phase difference between the two IFs, in order to preserve the relative coordinates between $v=1$ and $v=2$ masers. As the group delays vary with time, the relative phase differences between IFs also change, and need to be tracked to prevent loss of coherence. Furthermore we found that the calibrator phases, which are changing essentially randomly between the hourly scans, could disrupt the phase connection across the 300-MHz spanned bandwidth by introducing different number of phase ambiguities at each IF and reduce the success rate for accurate phase tracking. Zeroing the calibrator phase entries is not a solution, since they also carry information on the relative phase difference between the IFs, as derived from the group delay estimates. In the *modus operandi* of AIPS, the group delays are stored as an IF-based delay entry, common for each IF, which represents the rate of change, and a phase entry for each IF derived from that delay and its difference to the reference frequency. Then, the calibrator phases at the reference frequency are added to those (delay related) phase entries.

To solve the problem with introducing extra phase ambiguities across the 300-MHz, we exported the solution table produced by FRING on the calibrator data set, and zeroed

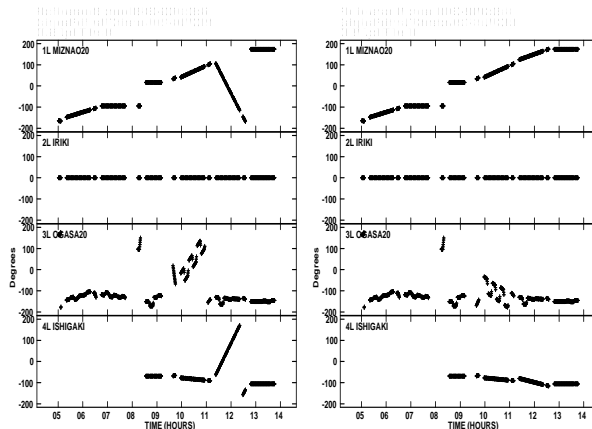


Fig. 3. Differences between antenna-based phase solutions for IFs separated by a frequency gap of ~ 300 MHz, at epoch IV. The phase entries have been estimated with FRING at the times of the \sim hourly continuum calibrator scans, on beam B, and interpolated to the times of RLMi observations (on beam A). *Left* and *Right* plots show the phase differences before and after removing the phases from the calibrator, respectively, whilst retaining the inter-IF terms derived from the group delay (see text). When the calibrator phase terms are not removed the expected, smooth phase connection between calibrator scans is occasionally broken. At the analysis, equally good results can be obtained using our scripts, or by subtracting out the phases from the reference IF.

the rate and the phase entries for the selected reference frequency (chosen at 43 GHz); also, we recalculated the phase entries for the rest of IFs from its difference with the reference frequency and the estimated delay. This ensured that the phases deduced from the delays could be transferred across the ~ 300 MHz between the two observed SiO maser transitions. If this was not done, the phase connection would occasionally breakdown (see Fig. 3). This problem affected to about 20% of the observing time in our data sets. These extra steps ensured unambiguous phase connection across the total duration of the observations and preserved the alignment between the SiO maser transitions.

Subsequently we have realized that part of the handling of the SN table can be done using the AIPS task SNCOR, with mode REFP, on a central IF. This approach has the advantage of not having to work outside the AIPS environment. Nevertheless we are happy to provide our perl script on request, as it also will phase center on an arbitrary frequency (useful when the reference IFs for beam A and beam B are not at the same frequency), and expand or contract the SN table for the different numbers of IFs allocated to beams A and B.

Then, we applied spectral line self calibration and imaging techniques on a compact and bright reference maser spot in the $v=2$ dataset, to track the short term atmospheric fluctuations and get a map of the feature. At each epoch, the resulting antenna-based phase and rate

solutions from a reference channel in the $v=2$ IF were used to calibrate all other $v=2$ spectral channels (the usual case) and also all $v=1$ channels in the other IF without separate $v=1$ reference channel calibration. The phase-referenced visibilities (of all velocity channels) were Fourier transformed using the AIPS task IMAGR, without further calibration, to yield image cubes of $v=1$ and $v=2$ SiO masers that preserve the relative astrometric registration with respect to the reference spot (in $v=2$).

This method allows relative astrometric alignment of the two frequencies, even if the maps have no absolute coordinates, largely thanks to the instrumental stability of the digital receiving system in VERA. The astrophysical results obtained from the maps and its astrometric alignment are presented in the next section.

This method would be expected to work when the errors introduced by uncertainties in the correlator model, the temporal interpolation between calibrator observations, and the extrapolation between different directions in the sky (5.9° away) and across the ~ 300 MHz spanning bandwidth between both transitions are reasonably small. We are confident that the interpolation between calibrator observations worked well because 4C39.25 (J0927+3902) was also occasionally observed in beam A, and we get a relative astrometric alignment between the maps of the two IFs, ~ 300 MHz away, of < 0.1 mas. This is of course on the same source from which we derive the delays, but at different times and with a different receiver. The uncertainties related to the spatial extrapolation result from unmodelled terms related to the atmospheric contribution, and source position errors. While the former will degrade the results adding noise, the latter propagates into the analysis as a systematic shift in the astrometric measurements between two SiO transitions maps.

There have been attempts to transfer the solutions between the $v=1$ and 2 maser transitions before, e.g. Boboltz & Wittkowski (2005) using observations with only two 8-MHz IFs. The concern is that, because of the narrow bandwidths and the low accuracy of the estimated delays, the relative phase between the two transitions might not be preserved. Yi et al. (2005) describe a wideband method, very similar to ours, which covers the 300-MHz span. Their attempt, however, failed because of the poor accuracy of the coordinates of the star observed, TX Cam. This led to a systematic relative error between the $v=1$ and $v=2$ positions of about 2mas. They, therefore, assumed a common feature for the two SiO maser transitions and derived the absolute position of TX-Cam. If an independent position had been available the same analysis as ours could have been applied. In our case we have observed a wide bandwidth to ensure that the delay errors are small, and both sources have positions measured with high precision astrometry (Hipparcos for RLMi, and VLBI for 4C39.25), with accuracies better than 1 mas. However the uncertainty in the proper motion of the line source, given that the Hipparcos observations were made in the early 1990's, results in a position error of the order of 30mas. We assume this is the dominant source of errors in our analysis and will use it to determine the final error bars in our astrometric measurements. An absolute position error of R LMi of 50mas in

our analysis would propagate into less than 0.4mas in the relative shift between the transitions (result from multiplying the star’s position error by the phase-referencing attenuation factor, $\Delta\nu/\nu$). With all, we give a conservative estimate of the uncertainties in our measurements of the relative $v=1$ and $v=2$ maser positions, at all epochs, of 0.4mas.

4. Results and discussion

The map resulting from H₂O maser observations towards R LMi showed a single compact component which was slightly resolved and had an integrated flux density of 3 Jy. The simple structure in the maps along with the lack of astrometric information, due to the non-detection of the reference source, invalidate our attempt to align the H₂O and SiO maser emission in R LMi. Because of this we have only fully analysed one epoch of the H₂O maser observations, as shown in Table 1.

Figs. 4 to 8 show the relative astrometrically aligned VERA maps of $v=1$ and $v=2$ $J=1\rightarrow 0$ SiO maser emission towards R LMi at the 4 epochs of observations (see Table 1), except for epoch I in which only $v=1$ emission was observed. We present first a brief description of the maps followed by a discussion on the astrophysical implications. All the figures are made from the data cubes, for which the thermal noises are around 0.2 Jy/beam per channel in both the $v=2$ and $v=1$ datasets. We blanked all pixels less than 1 Jy/beam, and averaged over the regions in which there was significant emission.

Fig. 4 shows the map of $v=1$ maser emission at epoch I; the structure in the map is very simple, with two groups of features that we will refer to as the Northern and the Western clusters. The $v=2$ maser observations failed due to a technical problem.

Fig. 5 shows the relative astrometrically aligned maps of the $v=2$ and $v=1$ maser emission at epoch II, with respect to the strongest channel in $v=2$. The compact features, with a velocity of 10.4 km s⁻¹, seen at both transitions do overlap.

Fig. 6 shows the maps at epoch III, the most feature rich emission in both $v=1$ and 2, showing clusters to the North, East, West and (in $v=1$ only) the South. We have used these spots to draw a circle which represents the assumed ring of emission around the central star. This ring is not a fitted solution, and it serves as a useful guide to the eye for comparison between the spots distribution at different epochs (epochs III and IV). The three clusters seen in both transitions (in Fig. 6) all show significant spatial offsets between spots with common velocities. We recall that coincidence of spots from different transitions requires not only a negligible spatial offset, but also coincidence in LSR velocity. Both spatial offsets and velocities are shown in Fig. 6, with arrows that indicate the distance and direction between coincident spots at $v=1$ and $v=2$, and labels for the corresponding velocities. The arrows head size corresponds to the estimated relative position errors in our astrometric analysis. The spots of the four regions with common emission at $v=1$ and 2 (two in the North and one each in the Western and Eastern clusters) do not overlap. The size of the spatial offsets between both

transitions is of several mas, except for the feature at -9.5 km s^{-1} , with an offset of 0.5 mas , not much more than our estimated astrometric errors. However, as Fig. 7 (also epoch III) shows, this region has a complex emission structure, with possible overlapping regions very much outnumbered by those definitely not overlapping.

A map at epoch IV is shown in Fig. 8. It shows some emission in the Northern and Western regions. The observations are only 27 days apart from epoch III and, albeit with far fewer spots, the structure in epoch IV resembles the one in the map at epoch III. We have superimposed the same circle as appears in Fig. 6 for visual comparison between the maps.

In summary, we have identified a total of about 17 spots in the $v=1$ line and 21 spots in $v=2$ masers, from an inspection of the maps at epochs II, III and IV (where both $v=1$ and 2 masers were observed). Among them we find two spots which are coincident within the conservative astrometric estimates of uncertainties in our analysis, of 0.4 mas (the northern spot in epoch III, at -9.5 km s^{-1} LSR, and the dominant spot in epoch II). We note that, since the displacements between nearby spots of different transitions show in general very different directions and absolute values, an error in the alignment of the maps could not explain the poor spot coincidence.

Our astrometric results are consistent with previous approaches (Desmurs et al. 2000, Boboltz & Wittkowski 2005, Yi et al. 2005, Cotton et al. 2004, 2006, 2008), in that the radius of the $v=1$ is greater than the $v=2$. These papers do not discuss the $v=1,2 J=1 \rightarrow 0$ spot coincidences and limit themselves to the average ring radii, as they were based on less well founded map alignment procedures. Both maser emissions occupy roughly the same regions, but the respective spots are rarely coincident; in the observations presented in this paper only about 1/10 of the identified spots are coincident to within our error estimates (0.4 mas).

The percentage of spot coincidence had been used as an argument favoring radiative or collisional pumping mechanisms. Although existing models really do not address the probability of intense common spots for these maser lines, the lack of systematic coincidences tends to favor radiative pumping because the conditions required to pump both masers are more different in the radiative case than for collisional excitation (see details below and in the extensive discussion by Desmurs et al. 2000).

In the standard versions of both pumping schemes (see e.g. Bujarrabal & Nguyen-Q-Rieu, 1981; Lockett & Elitzur, 1992), the inversion of the $v=1$ and $v=2$ rotational transitions appear under quite different conditions. This is due to the different excitation required in both cases: the $v=1$ state is at 1800 K over the ground, while the $v=2$ one is at 3600 K . Therefore, different (always high) excitation would be required and both masers can rarely coexist in both models. In the radiative model, the coincidence is somewhat less probable than for the collisional pumping. For instance, Bujarrabal & Nguyen-Q-Rieu estimate that in the radiative model the $v=2$ maser pumping needs a density about 5 times larger than for the $v=1$, while in the collisional scheme the factor is ~ 2.2 . This has led to a long-lasting discussion on the

consequences on theoretical modelling of the possible systematic coincidence of $v=1$ and $v=2$ $J=1\rightarrow 0$ spots. Both pumping mechanisms predict that masers of rotational transitions within the same vibrational state ($J=1\rightarrow 0$, $J=2\rightarrow 1$, etc) must be strongly coupled and should appear in practically the same points. More recent theoretical studies address the general relative distributions of the different maser spots, i.e. the ring radii for the various lines. Humphreys et al. (2000, 2002) explains the slightly larger radius found for the $v=1$ $J=1\rightarrow 0$ maser assuming collisional pumping driven by shocks; in their calculations the $v=1$ $J=2\rightarrow 1$ ring is practically identical to the $v=1$ $J=1\rightarrow 0$ one, as expected. Soria-Ruiz et al. (2004) can also explain the difference observed between the two $J=1\rightarrow 0$ lines under the radiative excitation framework; in this model, the position of the $v=1$ $J=2\rightarrow 1$, 86-GHz maser may vary depending on some possible alteration of the radiative pumping (see below).

Our understanding of these problems has greatly changed from the first empirical comparisons between $v=1$ $J=1\rightarrow 0$ and $J=2\rightarrow 1$ maser distributions (Soria-Ruiz et al. 2004, 2005, 2007). The $v=1$ $J=2\rightarrow 1$ maser spots also occupy a ring, but are systematically placed at a much larger distance from the star than those of $v=1$ $J=1\rightarrow 0$, and both spot distributions are completely different.

Soria-Ruiz et al. (2004) explained these results invoking the effects of line overlap between the $(v=1, J=0) - (v=2, J=1)$ rovibrational transitions of SiO and the $(v_2=0, 12_{7,5}) - (v_2=1, 11_{6,6})$ rovibrational line of H_2O (see also Olofsson et al. 1981, Bujarrabal et al. 1996). Their calculations indicate that the overlap of these infrared lines reinforces the $v=1, 2$ $J=1\rightarrow 0$ masers; the quenching of the (otherwise intense) $v=2$ $J=2\rightarrow 1$ maser is also predicted, in agreement with observations. The overlap also introduces a strong coupling between $v=1, 2$ $J=1\rightarrow 0$ masers, that now must appear under very similar conditions. Meanwhile, the $v=1$ $J=2\rightarrow 1$ maser is expected to be less affected by this phenomenon and to show practically no relation with the two 43-GHz lines. The calculations by Soria-Ruiz et al. (2004) are in agreement, at least qualitatively, with all existing data on the relative large-scale distributions of the different SiO maser lines. In our opinion, at the moment it is not possible to understand the general properties of the maps of SiO maser maps without taking into account those theoretical considerations on the effects of line overlap.

We have seen that the results of radiative pumping models including line overlap, as proposed by Soria-Ruiz et al. (2004), are compatible with these (and other) observational results on SiO maser distribution. But these models serve to understand the general distribution of the SiO maser brightness, not to predict the coincidence probability of the very intense and compact spots detected in VLBI experiments. For such a purpose, we must understand the competition between different maser lines under conditions of extreme maser saturation, an intricate phenomenon that will be very difficult to quantify. Therefore, we still lack for specific theoretical studies on the probability of detecting, in both $v=1$ and $v=2$ $J=1\rightarrow 0$, spots with very high brightness, which is the true parameter to be compared with the spot coincidence ratio

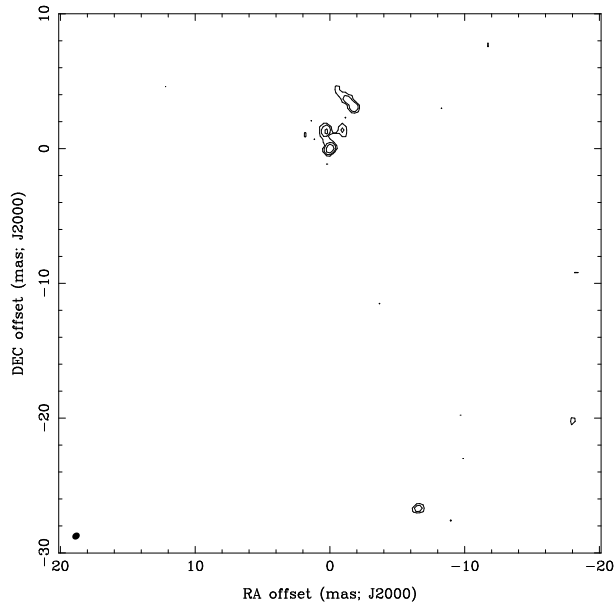


Fig. 4. Contour map of SiO $v=1$ $J=1 \rightarrow 0$ maser emission in RLMi in epoch I, averaged over regions with significant emission. The contours are at 1, 2, 4 and 6 Jy/beam. The noise levels in the cube were 0.2 Jy/bm/channel.

we can deduce from the observations. In summary, the very last observations, made in response to the questions posed by the different theoretical models, are now leading the modelling, and further efforts are required to address the observational results. In these efforts the capabilities of VERA, both for relative and absolute astrometry, will facilitate major advances in the observations of SiO masers.

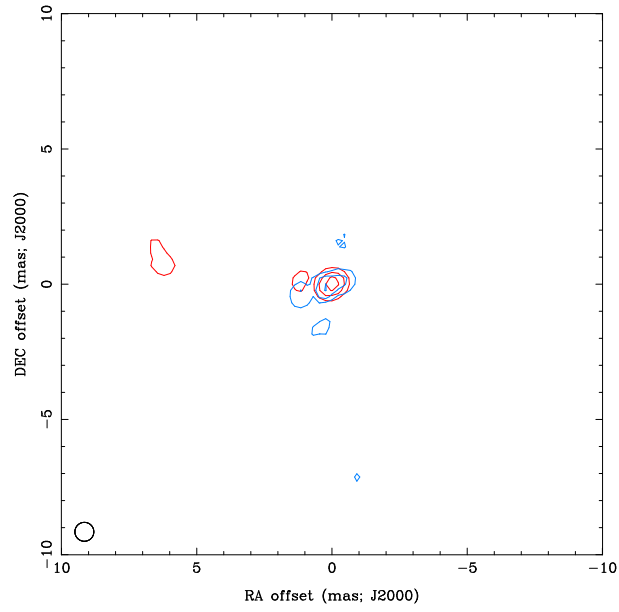


Fig. 5. Relatively astrometrically aligned contour maps of $v=1$ (red; less intense lines) and $v=2$ (blue) $J=1\rightarrow 0$ SiO maser emission towards RLMi, with respect to the position of the strongest channel in $v=2$, at epoch II. The contours are at 3, 6 and 10 Jy/beam. The noise levels in the cubes were 0.2 Jy/bm/channel.

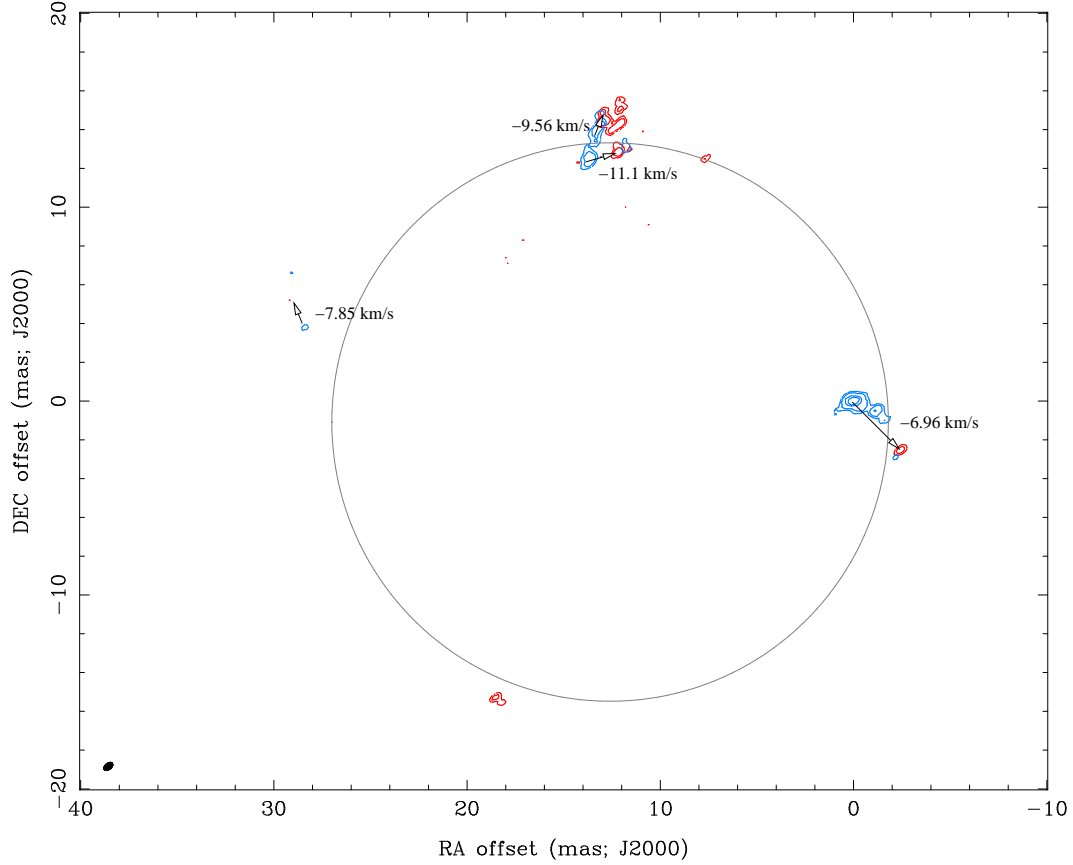


Fig. 6. Relatively astrometrically aligned contour maps of $v=1$ and $v=2$ $J=1 \rightarrow 0$ SiO maser emission towards RLMi, with respect to the position of the strongest channel in $v=2$, at epoch III. We used the same colors as in previous figure. The contours are 2, 3, 6, 8 and 10 Jy/beam. The noise levels in the cubes were 0.2 Jy/bm/channel. The circle approximates the assumed ring of emission around the central star; it is not a fitted solution, and serves for visual comparison of the spatial distribution of spots at different epochs. The arrows indicate the relative position between nearby spots of $v=2$ and $v=1$ masers with common velocities. The size of the arrows head corresponds to our conservative estimate of the errors in the astrometric alignment between the $v=1$ and 2 maser maps (see text).

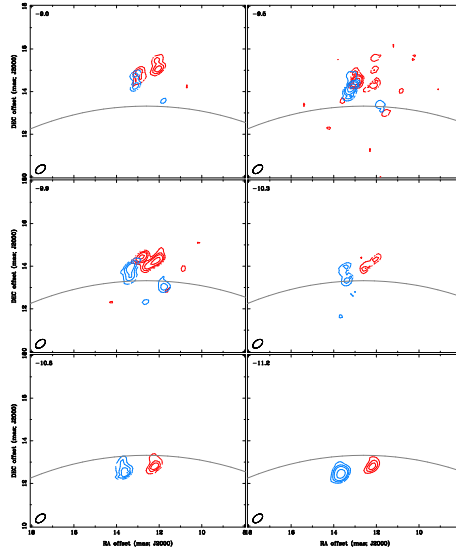


Fig. 7. Detail of the epoch III map shown in Figure 6 (Northern cluster), with the channels averaged to 4.4 km s^{-1} . The colors are as before. One can see that, whilst there is one cluster with common velocity and position, none of the others overlap. Contours are at 2, 3, 4, and 6 Jy/beam.

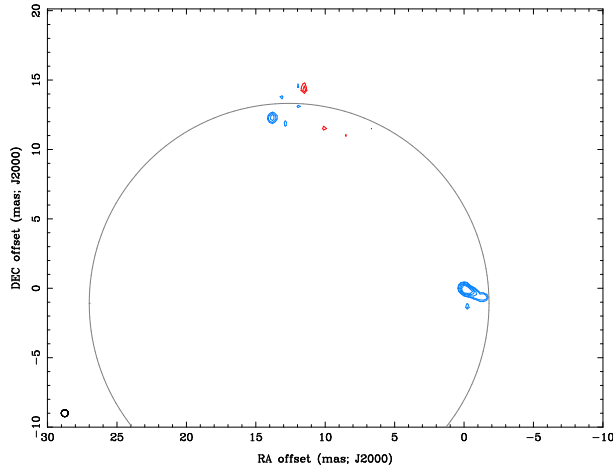


Fig. 8. Relatively astrometrically aligned contour maps of $v=1$ and $v=2$ $J=1 \rightarrow 0$ SiO maser emission towards RLMi, with respect to the strongest channel in $v=2$, at epoch IV. The colors are as in previous figures. The contours, for $v=2$, are at 3, 4, and 6 Jy/beam and, for $v=1$, are 3, 4, 6, 8, 10 Jy/beam. The circle aims to be of help for a visual comparison of the spots distribution between epochs (see text). The noise levels in the cubes were 0.3 Jy/bm/channel.

Acknowledgements

We would like to thank the VERA team for their support with the observations. We acknowledge support from the *Spanish Ministry of Education & Science*, under grant PCI2005-A7-0246. Richard Dodson acknowledges support as a Marie-Curie fellow via EU FP6 grant MIF1-CT-2005-021873. We are grateful to Riccardo Cesaroni for providing single dish measurements of water maser emission in several sources, which were useful to prepare the observations. We acknowledge with thanks the variable star observations from the AAVSO International Database, contributed by observers worldwide and used in Figure 1. We would like to thank the anonymous referee for the comments to this paper.

References

- Boboltz, D. A., & Wittkowski, M. 2005, *ApJ*, 618, 953
 Bujarrabal, V. 1994, *A&A*, 285, 971
 Bujarrabal, V., & Nguyen-Q-Rieu 1981, *A&A*, 102, 65
 Bujarrabal, V., Alcolea, J., Sanchez Contreras, C., & Colomer, F. 1996, *A&A*, 314, 883
 Chikada, Y., Kawaguchi, N., Inoue, M., Morimoto, M., Kobayashi, H., Mattori, S., 1991, in *Frontiers of VLBI*, ed. H. Hirabayashi, M. Inoue, & H. Koybayashi (Tokyo: Universal Academy Press), 79
 Cotton, W. D., Perrin, G., & Lopez, B. 2008, *A&A*, 477, 853
 Cotton, W. D., et al. 2006, *A&A*, 456, 339
 Cotton, W. D., et al. 2004, *A&A*, 414, 275
 Desmurs, J. F., Bujarrabal, V., Colomer, F., & Alcolea, J. 2000, *A&A*, 360, 189
 Humphreys, E. M. L., Gray, M. D., Yates, J. A., Field, D., Bowen, G., & Diamond, P. J. 2000, *EVN*

- Symposium 2000, Proceedings of the 5th european VLBI Network Symposium, 197
- Humphreys, E.M.L., Gray, M.D., Yates, J.A., et al. 2002, A&A, 385, 256
- Lockett, P., & Elitzur, M. 1992, ApJ, 399, 704
- Olofsson, H., Hjalmarson, A., & Rydbeck, O. E. H. 1981, A&A, 100, L30
- Pardo, J. R., Alcolea, J., Bujarrabal, V., Colomer, F., del Romero, A., & de Vicente, P. 2004, A&A, 424, 145
- Perryman, M.A.C., et al. 1997, A&A, 323, L49
- Soria-Ruiz, R., Alcolea, J., Colomer, F., Bujarrabal, V., Desmurs, J.-F., Marvel, K. B., & Diamond, P. J. 2004, A&A, 426, 131
- Soria-Ruiz, R., Colomer, F., Alcolea, J., Bujarrabal, V., Desmurs, J.-F., & Marvel, K. B. 2005, A&A, 432, L39
- Soria-Ruiz, R., Alcolea, J., Colomer, F., Bujarrabal, V., & Desmurs, J.-F. 2007, A&A, 468, L1
- Whitelock, P., Marang, F., & Feast, M. 2000, MNRAS, 319, 728
- Yi, J., Booth, R.S., Conway, J.E., Diamond, P.J., 2005, A&A, 432, 531